IEEE Access
Multidisciplinary ⋮ Rapid Review ⋮ Open Access Journal

Received 8 February 2024, accepted 5 March 2024, date of publication 12 March 2024, date of current version 18 March 2024.

Digital Object Identifier 10.1109/ACCESS.2024.3374896

RESEARCH ARTICLE

Dual-Band MIMO Prototype in the Sub-6 GHz Integrated With mm-Wave Arrays: Ensuring Beamforming and Safety Measures

AYESHA KAZMI[1], MUHAMMAD ZADA[2], (Member, IEEE), SAIFUL ISLAM[3], (Graduate Student Member, IEEE), AND HYOUNGSUK YOO[3], (Senior Member, IEEE)

[1]Department of Electrical Engineering, CECOS University of IT and Emerging Sciences, Peshawar 25000, Pakistan
[2]College of Electronics and Information Engineering, Shenzhen University, Shenzhen 518060, China
[3]Department of Electronic Engineering, Hanyang University, Seoul 04763, Republic of Korea

Corresponding author: Hyoungsuk Yoo (hsyoo@hanyang.ac.kr)

This work was supported by the Institute for Information and Communications Technology Promotion (IITP) grant funded by the Korean Government [Ministry of Science, and Information and Communications Technology (ICT) and Future Planning (MSIP)] under Grant 2022-0-00310.

ABSTRACT In response to the increasing demands for 4G LTE and 5G smartphone applications, this study presents a compact and integrated prototype designed to cover sub-6 GHz and 5G mm-wave bands with high-frequency ratios. The proposed integrated design incorporates two multiple-input-multiple-output (MIMO) configurations: a 2 × 2 dual-band planar inverted-F antenna (PIFA) MIMO for sub-6 GHz and an array of eight elements for mm-wave. Proximity placement (2.5 mm separation) of mm-wave elements on smartphone RIM achieves compact array size with optimal beamforming, coverage, and interference prevention. Utilizing a meandered patch and truncated ground, the proposed PIFA achieves a size of 37 mm × 7 mm × 0.508 mm with a Rogers RT/Duroid 5880 substrate. Effective operation is demonstrated in sub-6 GHz bands (5G at 3.8 GHz, LTE band-46 at 5.4 GHz), complying with safety standards (specific absorption rate and power density) set by the Institute of Electrical and Electronics Engineers and the International Commission on Non-Ionizing Radiation Protection. Efficient performance extends to the 5G mm-wave band at 28 GHz, making it a promising choice for modern smartphone applications.

INDEX TERMS 4G LTE, 5G mm-wave, MIMO configurations, planar inverted-F antenna (PIFA), safety analysis, smartphone applications.

I. INTRODUCTION

Mobile communication, a pervasive element of daily life and one of the most dynamic realms of social development stands at the forefront of technological evolution [1]. In response to the rapid surge in data and information, modern wireless networks demand high-speed data rates with low latency. This imperative need has spurred the continuous development of wireless communication technologies, with the 4th Generation of Communication (4G), known as Long Term Evolution (LTE), leading the way by providing superior data rates and throughput [2]. However, existing sub-6 GHz wireless communication technologies, such as 4G and WiFi, face congestion issues, restricting bandwidth and supporting only modest data rates [3]. To address this, the next-generation technology, 5G, requires a novel spectrum allocation mechanism allowing wider bandwidth [4]. The International Telecommunication Union and Federal Communication Commission (FCC) propose the mm-wave band with a minimum of 500 MHz bandwidth for 5G applications, prompting researchers to explore the mm-wave spectrum for its wider bandwidth and potential for higher data rates than sub-6 GHz bands [5], [6], [7]. However, electromagnetic waves in the mm-wave spectrum encounter

The associate editor coordinating the review of this manuscript and approving it for publication was Muhammad Zubair.

challenges like multipath fading and atmospheric absorption losses [8]. Researchers propose multiple-input-multiple-output (MIMO) and antenna arrays as solutions to overcome these limitations. Antenna arrays offer high gain, while MIMO technologies enable higher capacity with multi-Gbps throughput [9], [10]. However, addressing isolation between multiple antennas becomes crucial and degrades device performance. Consequently, designing MIMO antenna arrays with high isolation, gain, and bandwidth necessitates the adoption of various isolation reduction techniques [11]. Therefore, designing multiband intrinsically isolated MIMO antenna systems is crucial.

For compact wireless terminals with constrained interior spaces, including smartphones, laptops, wearable gadgets, and vehicles, the demand for cost-effective antennas capable of concurrently supporting multiple frequency bands is pressing [12]. Consequently, the imperative arises for seamless integration and compatibility between the established sub-6 GHz technology and the emerging mm-wave technology. Within the context of the 5G heterogeneous network [13], legacy technologies in the sub-6 GHz range ensure low-latency basic coverage, voice, and signaling for mobile users. By contrast, mm-wave cells step in to provide unparalleled capacity when required. This necessitates antenna capability to operate seamlessly in both mm-wave and sub-6 GHz frequency bands. However, owing to the substantial frequency gap between the sub-6 GHz and mm-wave bands, conventional techniques employed for multiple band antennas in these ranges prove unsuitable for MIMO applications. Consequently, the quest for innovative methods to maximize limited space with multiband antennas becomes a central focus of extensive research interest.

In the past decade, significant efforts have been directed towards developing integrated antennas [14], [15], [16], [17]. To accommodate 2G, 3G, 4G, and 5G technologies in a limited space, researchers have utilized various antenna types, including patch [18], monopole [19], [20], dipole [21], [22], [23], slot [24], [25], [26], and planar inverted-F antennas (PIFAs) [27]. These designs attempted to realize multiple bands required to integrate these standards. Some studies successfully achieved low-profile and wideband characteristics suitable for portable devices. However, these works primarily focused on integrating sub-6 GHz bands and faced challenges accommodating mm-wave 5G bands. Unlike integrating multiple bands within the sub-6 GHz range, creating a 5G MIMO antenna array with satisfactory isolation and a compact size for current smartphones proves a formidable challenge, particularly at lower frequencies. Several studies have addressed this challenge through the codesign of dual-band or multifrequency antennas with a large frequency ratio [28], [29]. However, these approaches may have drawbacks, including limitations on feed positions, intricate feeding methods, and the enlargement of radiating structures for sub-6 GHz antennas. These factors pose challenges for implementing MIMO configurations at lower frequency bands.

This study presents an integrated prototype designed to cover the sub-6 GHz (mid-band) and 5G mm-wave bands, specifically tailored for 4G LTE and 5G smartphone applications. The proposed design incorporates two distinct MIMO configurations for both bands; a 2×2 MIMO configuration was constructed for sub-6 GHz antennas on two short edges of the substrate and two arrays of eight antenna elements were designed on the rim of the long edges of the substrate for the mm-wave configuration. By positioning these elements near a separation of 2.5 mm, we can achieve optimal beamforming characteristics to provide coverage on both sides, prevent interference with antennas utilized for other applications, and attain high gain and isolation. Utilizing a meandered structure for the patch and a truncated ground structure, we achieved a compact size of 37 mm $\times$ 7 mm $\times$ 0.508 mm for the proposed dual-band PIFA, employing the Rogers RT/Duroid 5880 substrate. Within the sub-6 GHz frequency bands, the proposed design effectively operates in the sub-6 GHz resonance frequencies for 5G at 3.8 GHz and LTE band-46 at 5.4 GHz. Moreover, at sub-6 GHz bands, a specific absorption rate (SAR) was analyzed, while at the high-frequency band, a power density (PD) analysis was performed for user safety reasons. The safety restrictions advised by the Institute of Electrical and Electronics Engineering (IEEE) and the International Commission on Non-Ionizing Radiation Protection (ICNIRP) were satisfied by achieving lower PDs and SARs. In addition, the design demonstrates efficient operation in the 5G mm-wave band of 28 GHz. Beyond its extensive bandwidth coverage, the proposed architecture underwent meticulous scrutiny to evaluate single and MIMO antenna performance. The parameters for the high performance of the antenna and adept MIMO characteristics position the proposed design as a promising candidate for modern smartphone applications in both sub-6 GHz and 5G mm-wave frequencies.

II. METHODOLOGY

A. PROPOSED MIMO CONFIGURATION DESIGN

The proposed MIMO configurations for the sub6-GHz and mm-wave antenna arrays are shown in Fig. 1. A 2×2 MIMO configuration was formed for sub-6 GHz antennas on two short edges of the substrate. sub-6 GHz Ant-1 was placed on the top short edge, while sub-6 GHz Ant-2 was placed on the lower short edge of the substrate to prevent the occupation of space by antennas for other applications. For the mm-wave configuration, two building blocks with eight antenna elements per block were formed on the RIM of the long substrate edges to provide both side coverage with beamforming capabilities. The first eight element blocks consist of A-1-A-8 on the RIM of the right-side long edge and others from A-9-A16 on the left side of the RIM of the long edge of the substrate to generate both side coverage. Several studies designed 8, 10, or 12 elements for 5G MIMO configurations. However, based on the modern smartphone, they are not applicable for mm-wave because they cover the whole long side edges of the smartphone, which is

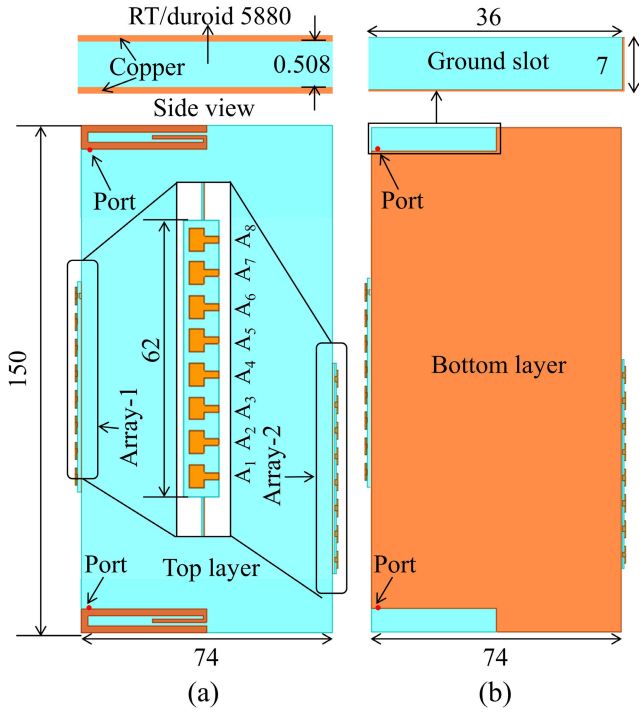

FIGURE 1. Geometry of proposed MIMO integrated sub-6 GHz and mm-wave antennas: (a) Front view including detailed and (b) rear view (units: mm).

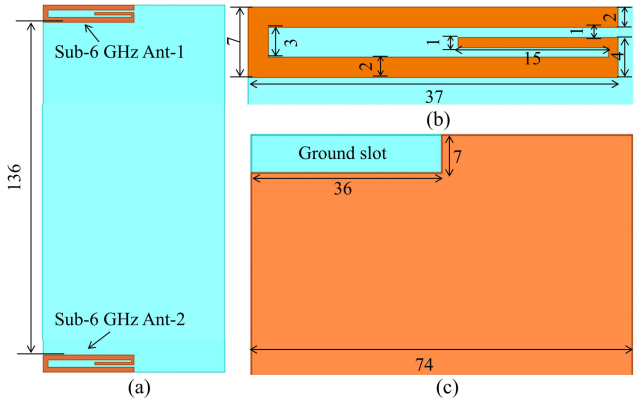

FIGURE 2. Geometry of sub-6 GHz PIFA: (a) Top surface with 2 × 2 MIMO configuration of PIFA, (b) PIFA geometry with detailed dimensions, and (c) cut view of 2 × 2 MIMO ground surface, (units: mm).

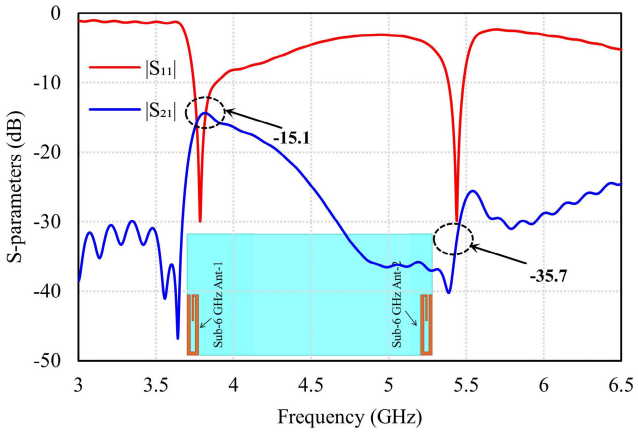

FIGURE 3. S-parameters of proposed dual-band PIFA with a 2 × 2 MIMO configuration before integration with mm-wave antenna arrays.

not practical as it requires whole metal frame clearance. Thus, for better space utilization, less metal frame clearance, and optimum isolation, the mm-wave elements were closely placed at a distance of 2.5 mm, less than a quarter wavelength. Eight elements were placed in a compact space of 58.3 mm. All the sub-6 GHz were printed on the front surface of the substrate, while the mm-wave antenna elements were printed on both sides of the smartphone RIM. We selected the Rogers RT/Duroid 5880 substrate with a dielectric constant $\varepsilon_r = 2.2$, loss tangent of $\tan\delta = 0.0009$, and thickness of 0.508 mm applied to the substrate. The substrate type and thickness were chosen to compensate for the fabrication capability and losses in the mm-wave bands. However, other materials having high dielectric properties have more losses at higher frequencies. The typical smartphone size with dimensions of 150 mm × 74 mm was applied to the substrate. On the back surface of the substrate, a full ground plane was applied with a clearance of 37 mm × 7 mm for the sub-6 GHz antennas at the top and bottom of the ground plane. CST microwave studio and HFSS simulators were utilized to design and analyze the proposed antenna configuration for smartphone applications. However, PD for the safety of smartphone users at 28 GHz was analyzed in the FDTD Sim4life software.

B. DESIGN OF DUAL-BAND SUB-6 GHZ PIFA

The structure of the proposed dual-band PIFA with a 2 × 2 MIMO configuration is illustrated in Fig. 2(a). The detailed structure of the dual-band PIFA and a defected ground plane are illustrated in Figs. 2(b) and 2(c) with its dimensions. The proposed antenna was constructed in a G-shaped spiral to generate two sub-6 GHz resonance frequencies for 5G at 3.8 GHz and LTE band-46 at 5.4 GHz. These resonances were achieved with a compact size of 37 mm × 7 mm. Compactness with dual-band characteristics was achieved by meandering the radiating structure into a G-shape. Notably, the meandering patch is a miniaturization technique adopted to downsize the antenna dimensions [30]. Despite assessment in miniaturization, the rectangular meandering structure also provides high isolation and very low envelop correlation coefficients (ECC) [1]. The meandering structure helped to smooth the current flow, which reduces the coupling and lowers the ECC. The meandering of the radiating structure extends the current path. Consequently, it lowers the resonant frequency. The initial dimensions were chosen based on the electrical length of the radiator according to the wavelength at a lower resonance frequency of 3.8 GHz. The permittivity of the dielectric material, denoted as ε_r and equal to 2.2 for Rogers RT/Duroid 5880, was considered in the design process.

Furthermore, to fit the antenna easily in the specified spaces inside the modern smartphone without occupying space of other application antennas, PIFA was designed in a

compact size of 37 mm × 7 mm. Moreover, these dimensions are enough to generate resonance at desired frequency bands. The top and bottom strips of the proposed PIFA have a width and length of 2 mm and 37 mm, respectively. Meanwhile, the width of the central strip and its adjacent gaps were limited to 1 mm to generate capacitive and inductive characteristics for impedance matching. A compressive parametric analysis was performed on the width and length of the strip and gap to achieve impedance matching at the frequency bands of 3.8 and 5.4 GHz. A 50Ω excitation signal was applied to a line going through the radiating patch to the ground plane at the bottom edge of the PIFA. For disposing of both PIFA for exciting the dual-band features to generate 3.5 GHz (sub6- GHz 5G) and LTE-46 bands, two rectangular ground clearance regions with dimensions of 36 mm × 7 mm were created at the top and bottom edges of the ground plane. Moreover, the ground slot also played a vital role in tuning and impedance bandwidth improvement. The performance of the 2 × 2 PIFA MIMO before integrating with mm-wave antenna arrays was evaluated in terms of reflection and transmission coefficients, as demonstrated in Fig. 3. Owing to symmetrical configuration, Fig. 3 only shows the s-parameters of a single PIFA, which is working at two resonances: one at 3.8 GHz and the other at 5.44 GHz. The reflection coefficients of the 2 × 2 PIFA MIMO ($|S_{11}|$ and $|S_{22}|$) were the same; thus, only $|S_{11}|$ was presented in the figure. At both frequencies, the resonance depths are equal to −30 dB, thus the PIFA is well-matched at these bands. Single antenna had −10 dB impedance bandwidth of 146 MHz (3.743-3.889 GHz) and 147 MHz (5.3563-5.5033 GHz) at lower and upper-frequency bands, respectively. Fig. 3 further illustrates the transmission coefficient ($|S_{21}|$) of 2 × 2 MIMO. The maximum mutual coupling between both the PIFAs was found to be −15.1 dB at 3.8 GHz, while −35.7 dB was found at the 5.4 GHz band. Moreover, the mutual coupling of the integrated antenna proposed here remained notably lower compared to several 5G antennas functioning in sub-6 GHz bands [1], [12], [31], [32], [33], and this was achieved without using decoupling structures and external circuits.

C. DESIGN OF MM-WAVE ANTENNA ARRAYS

We developed two arrays, each with eight antenna elements placed on the smartphone RIM at the long edges of the substrate to provide coverage on both sides. The top and bottom views of the substrate with mm-wave antenna arrays are shown in Figs. 4(a) and (b), respectively. Fig. 4(a) shows the detailed zoom view of a single element in the proposed mm-wave antenna array with detailed dimensions. Initially, a single antenna element was designed on the top surface of the separate substrate with dimensions of 62 mm × 8 mm × 0.508 mm. The size of the proposed mm-wave antenna for generating the 28 GHz resonance was obtained from equations in the literature [34].

The mm-wave antenna was designed based on the calculated values of all the antenna parameters. Further, the antenna was optimized to operate at 28 GHz with wide

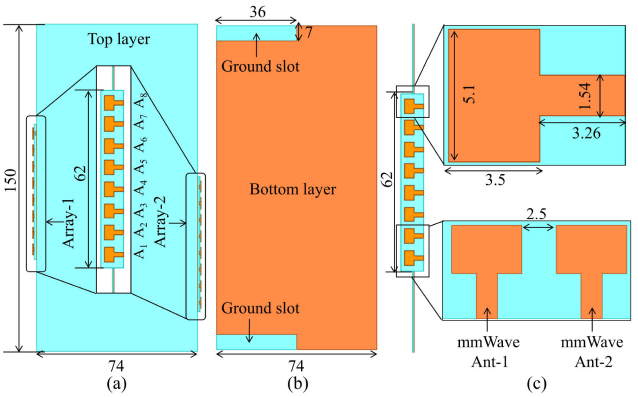

FIGURE 4. Geometry of mm-wave antenna arrays (units: mm). (a) Two arrays of eight elements are positioned on both sides of the smartphone RIM. (b) Ground surface with slots for PIFA. (c) Detailed geometry of mm-wave antenna and separation between two elements.

bandwidth characteristics in CST microwave studio software. After several parametric analyses, the optimized values for the W_p and L_p were 5.1 and 3.5 mm, respectively. Fig. 4(c) shows the single antenna element for mm-wave operation including its dimensions. After optimization, a building block with eight antenna elements having the same dimensions was developed on the long edges of the smartphone RIM. The two closest antenna elements were placed 2.5 mm apart, which is nearly equal to a quarter wavelength at 28 GHz, to provide lower mutual coupling values. The mm-wave antennas are directive in nature; thus, we have developed another block of eight elements on the other side of the substrate to cover both sides of the smartphone and imitate the array configuration. All the antenna elements were placed on the top surface of the substrate with dimensions of 62 mm × 8 mm × 0.508 mm, while a full ground plane with the same size was utilized on the backside to get optimum radiation performance for the 5G application. Each array of eight elements occupied a small size of 62 mm on the long edges of the substrate.

The reflection coefficient of the designed 5G mm-wave antenna elements is illustrated in Fig. 5. The designed single antenna element is well matched at 28 GHz with a resonance depth of -20 dB and a bandwidth of 1110 MHz covering the 5G range of 27.49-28.6 GHz. Furthermore, eight-element arrays were created in a symmetrical pattern, as illustrated in Fig. 1. Thus, the reflection coefficients were the same. The mutual coupling between the two closest elements ($|S_{21}|$, $|S_{32}|$) of the MIMO was -23.1 dB; however, in another element, it was decreased considerably owing to a large separation, as evident from $|S_{31}|$, $|S_{41}|$, $|S_{51}|$, $|S_{61}|$, $|S_{71}|$, $|S_{81}|$ in the figure. The isolation and bandwidth achieved were adequate for 5G smartphone applications.

III. RESULTS AND DISCUSSION OF INTEGRATED ANTENNAS

After all, the sub-6 GHz and mm-wave antennas were integrated on the same substrate with dimensions equal to those of commercial smartphones. The sub-6 GHz antennas for 5G and LTE were placed on the upper and lower side of

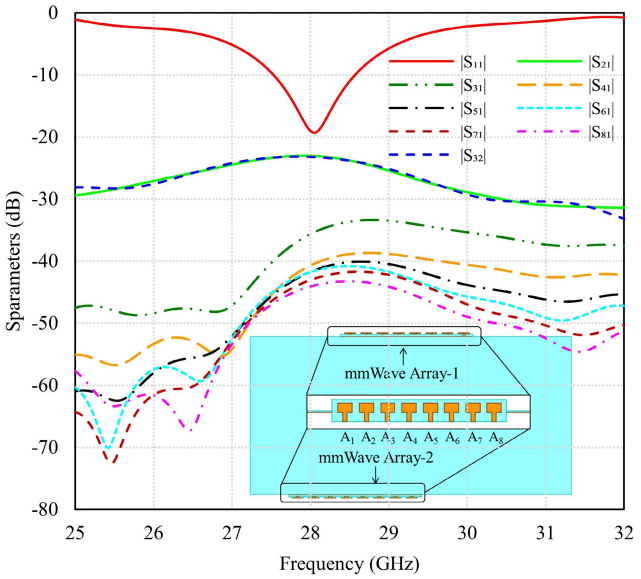

FIGURE 5. S-parameters of the mm-wave antenna array before integration with sub-6 GHz antennas.

the substrate. By contrast, the mm-wave antenna elements were placed vertically on the long edges of the substrate, as indicated in Fig. 1. The performance of the integrated antennas was evaluated in terms of current distributions, scattering parameters, gain, radiation patterns, and safety of the user from EM exposure. In addition, the MIMO performance was evaluated in terms of ECC and channel capacity between the sub-6 GHz MIMO elements, while the mm-wave arrays were studied for the beamforming characteristics.

A. PROTOTYPES OF PROPOSED INTEGRATED ANTENNAS

The proposed integrated antenna system is fabricated on an RT/Duroid 5880 substrate with specific material properties effective for high-frequency applications. The substrate has a dielectric constant (ε_r) of 2.2 and a low loss tangent (tanδ) of 0.0009, ensuring minimal signal attenuation. With a thickness of 0.508 mm, the substrate provides a compact yet robust foundation for the antenna design. The overall dimensions of the substrate measure 150 mm × 74 mm, closely resembling the form factor of existing smartphones. This size provides sufficient space to accommodate both the sub-6 GHz and 5G mm-wave components, ensuring compatibility with the compact design requirements of modern smartphones. The PIFAs are directly fabricated on the front side of the substrate, while the ground is established on the back side, optimizing the arrangement for efficient signal transmission and reception. Notably, the mm-wave arrays are manufactured separately on the same substrate, featuring dimensions of 62 mm × 8 mm × 0.508 mm. These arrays are then carefully attached to the original substrate, ensuring precise integration of the high-frequency elements to generate both side coverage. The fabricated prototypes of the proposed integrated antenna, including

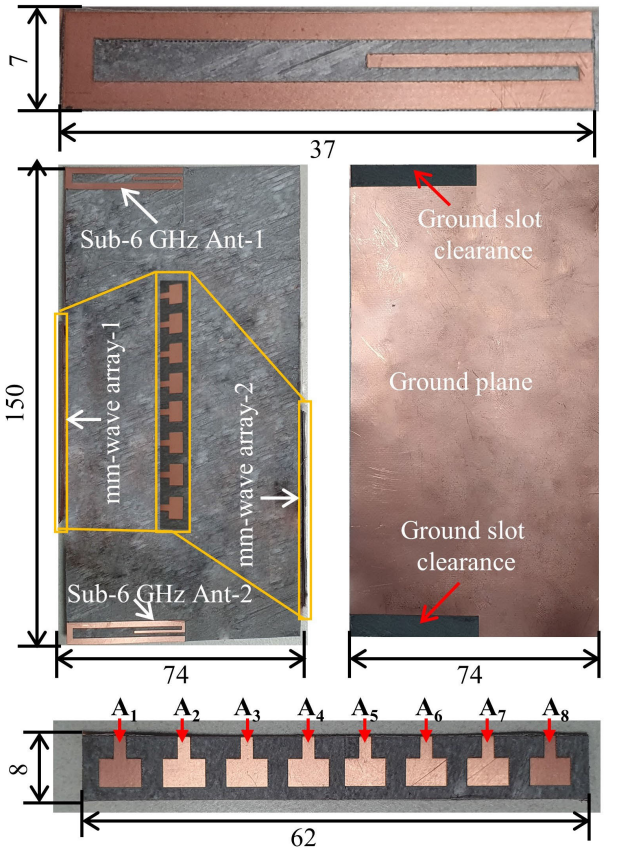

FIGURE 6. Fabricated prototypes of integrated antenna system on RT/Duroid 5880 substrate. Prototype resembles modern smartphones (150 mm × 74 mm) and accommodates sub-6 GHz and 5G mm-wave antennas. PIFAs (37 mm × 7 mm × 0.508 mm) are printed on the front, and mm-wave arrays (62 mm × 8 mm × 0.508 mm) are carefully attached on the RIM side vertically. Note: All dimensions are in millimeters.

their dimensions, are shown in Fig. 6. The entire fabrication process is executed with the LPKF ProtoLaser U4, a tool known for its precision and versatility in producing intricate antenna structures. This fabrication approach attempts to achieve optimal performance and reliability in catering to the demanding requirements of 4G LTE and 5G smartphone applications.

B. CURRENT DISTRIBUTIONS

Figs. 7(a) and (b) show the current distributions on the sub-6 GHz antennas at the 3.8 and 5.4 GHz resonance frequencies, respectively. The current distributions can help control the resonance frequencies and also show the coupling with nearby antenna elements. The zoomed view of the PIFA antenna at the sub-6 GHz 5G band and LTE band-46 was plotted on the top of Fig. 7. At 3.8 GHz, the antenna current path is longer, and the current density is higher at the lower longer part of the PIFA structure. However, the current path at 5.4 GHz becomes shorter owing to multiple direction changes, while the current density is higher at the top and bottom of the PIFA. Thus, we can control the impedance matching easily from the top surface of the G-shaped radiator

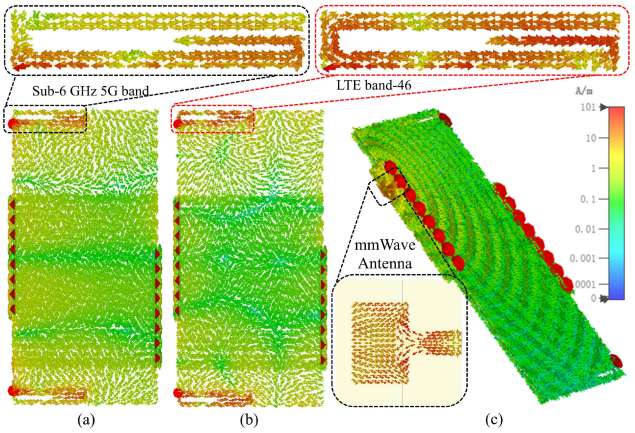

FIGURE 7. Current distribution of proposed integrated antennas: (a) Sub-6 GHz Ant-1 at 3.8 GHz, (b) sub-6 GHz Ant-1 at 5.4 GHz, and (c) Antenna element of Array-1 at mm-wave band of 28 GHz.

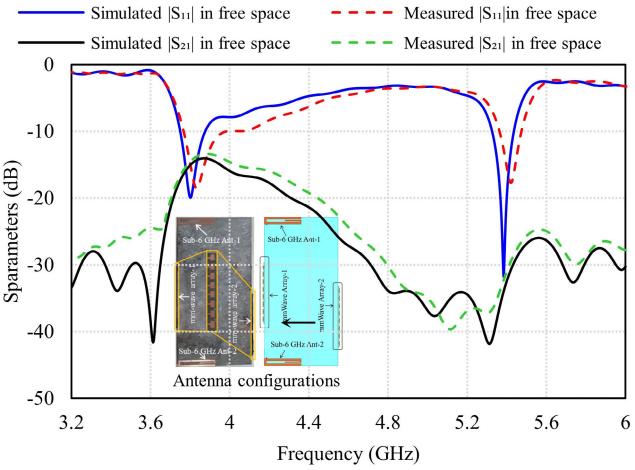

FIGURE 8. Comparing simulated and measured scattering parameters of integrated dual-band PIFA in the sub-6 GHz.

at a 5.4 GHz frequency band because, in the 3.8 GHz, the current density on the top surface of the G-shaped radiator is much lower. Similarly, the current distribution on the mm-wave array with a zoomed view of the antenna element at 28 GHz is plotted in Fig. 7(c). The current density is higher at the radiating patch of the mm-wave antenna and equally distributed over the patch, thus responsible for generating a single resonance at 28 GHz. The current density around the other elements is considerably lower, thus providing minimal mutual coupling between elements.

C. SCATTERING PARAMETERS

The simulated and measured reflection coefficients of the proposed dual-band PIFA for sub-6 GHz Ant-1 and sub-6 GHz Ant-2 after integration with mm-wave antenna arrays are shown in Fig. 8. It is evident that the proposed antenna provides dual-band characteristics at sub-6 GHz 5G bands of 3.8 GHz and LTE band-46 of 5.4 GHz. It is worth mentioning that the sub-6 GHz 5G bands usually work in the range of 3.6–4.1 GHz [35], whereas the LTE band-46 operates in the 5.150–5.925 GHz range [5]. However, most

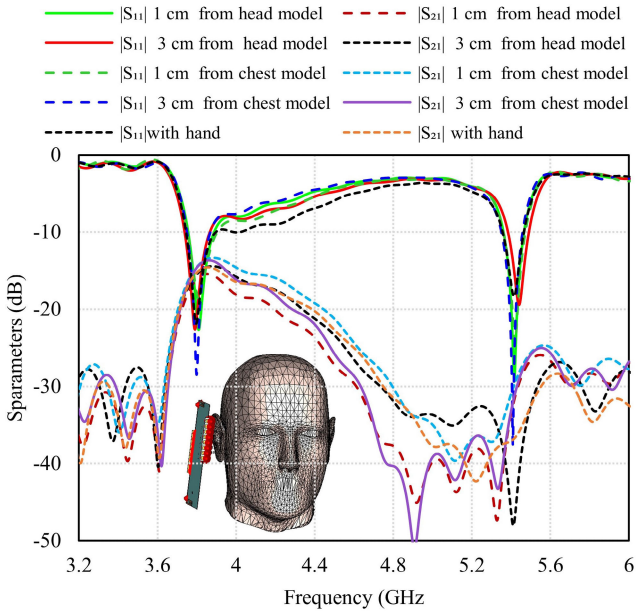

FIGURE 9. Simulated scattering parameters for integrated dual-band PIFA post-mm-wave antenna array integration. Human body proximity analysis reveals consistent resonance features as the antenna maintains dual-band characteristics for sub-6 GHz 5G (3.8 GHz) and LTE band-46 (5.4 GHz) with minimal resonance shift and low mutual coupling.

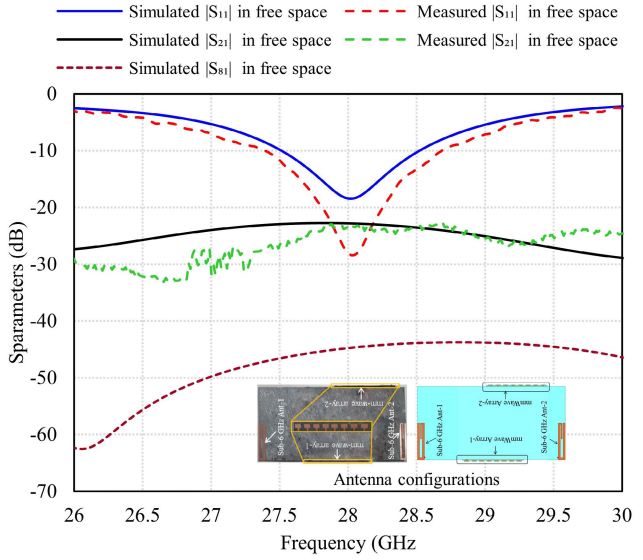

FIGURE 10. Comparing simulated and measured scattering parameters of the integrated antenna arrays in the mm-wave frequency range.

5G frequency bands differ from country to country. The proposed dual-band PIFA in the integrated form is working in the sub-6 GHz 5G band with a −10 dB impedance bandwidth of 144 MHz (3.743–3.887 GHz) and in the LTE band-46 with a bandwidth of 113 MHz (5.376–5.489 GHz). After integrating with the mm-wave antennas, the bandwidth at the lower band decreased by 2 MHz, and the higher frequency band decreased by 34 MHz owing to coupling. However, both frequency bands are well matched at the aforementioned frequency bands with resonance depths of −21.4 and −21.6 dB, respectively. Sub-6 GHz Ant-1 and sub-6 GHz

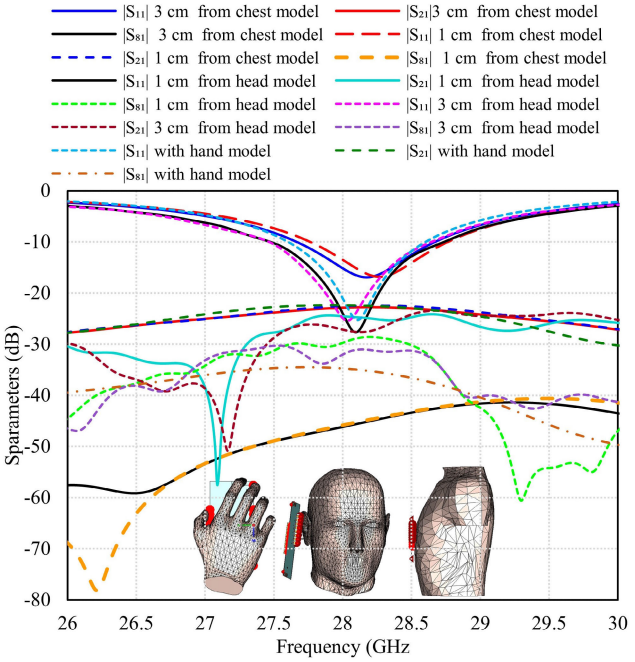

FIGURE 11. Scattering parameters of the proposed mm-wave antenna array. Figure highlights reflection and transmission coefficients, impedance matching, and mutual coupling characteristics of the mm-wave antenna array under various scenarios, emphasizing its resilience in proximity to human body models. Results highlight the stable performance of the antenna, including wide bandwidth and effective mutual coupling, crucial for 28-GHz applications in 5G technologies.

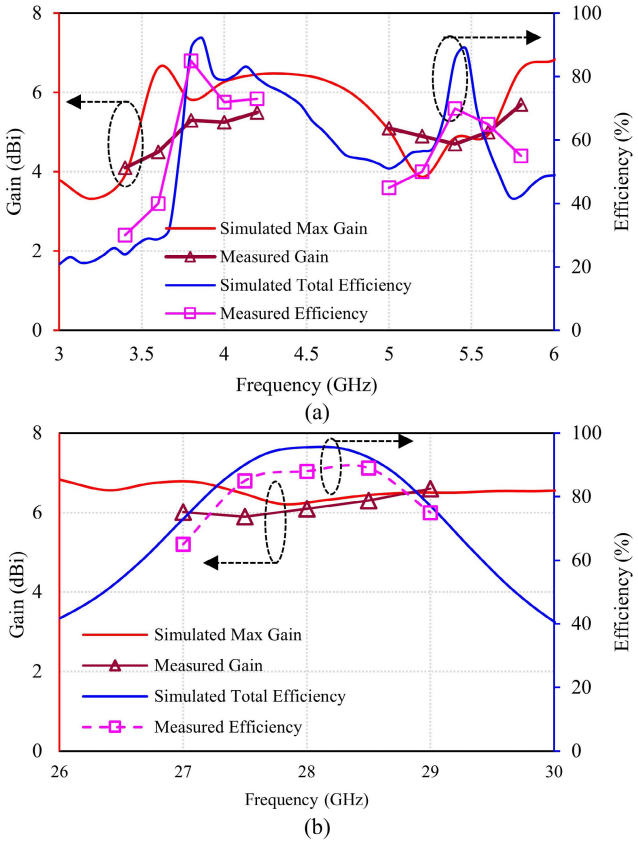

FIGURE 12. Comparative analysis of measured and simulated radiation performance in terms of total efficiency and maximum gain at (a) Sub-6 GHz frequencies and (b) mm-wave frequencies.

Ant-2 demonstrated the same bandwidth and impedance-matching performance. However, regardless of placement, mutual coupling is possible owing to sharing the same ground plane. Therefore, the transmission coefficient of sub-6 GHz Ant-1 and sub-6 GHz Ant-2 are also plotted in Fig. 8. Simulated mutual coupling of −15.72 and −35.71 dB were achieved in the free space at the 3.8 and 5.4 GHz resonances, respectively. Furthermore, the prototype of the proposed integrated antennas is measured for the s-parameters in free space, and a significant resemblance with simulation results was observed. Regardless of the shared ground plane, the proposed PIFA had prominent isolation in the sub-6 GHz frequencies compared to recent studies on 5G antennas for a smartphone application [1], [12], [15], [31], [32], [33].

Moreover, smartphones usually work near the human body, such as the head in talking mode, and the chest pocket and hand in data mode. Thus, we have further analyzed the effects on s-parameters of the human head, hand, and chest when the smartphone is 1 and 3 cm away from them. As illustrated in Fig. 9, the proposed integrated antennas provide dual resonance features at the desired resonance frequencies in all scenarios. However, a slight shift was observed when the antennas were close to the tissues owing to the human body's high dielectric tissues. Nevertheless, it can efficiently cover both 5G and LTE bands owing to its broadband features. Insignificant changes occurred in the mutual coupling values owing to the integration of mm-wave elements and placement in proximity with human body models.

The comparison of the simulated and measured reflection and transmission coefficients of the mm-wave antenna after integration are illustrated in Fig. 10. Similar to sub-6 GHz antennas, the mm-wave antennas also demonstrated decent performance in terms of impedance matching and wide bandwidth characteristics. The figure establishes that the mm-wave antenna in free space had a simulated bandwidth of 1040 MHz with a resonance depth of −18.2 dB at the 28 GHz band. All the elements had the same reflection coefficient owing to symmetrical placement and low coupling between the elements. Therefore, we have presented only a single antenna element reflection coefficient for brevity. Further, we analyzed the mutual coupling between the mm-wave antenna elements in the free space. In pursuit of brevity and owing to symmetrical placement, the mutual coupling ($|S_{21}|$ and $|S_{81}|$)between Ant-1, Ant-2, and Ant-8 of mm-wave Array-1 are shown in Fig. 10. As the other eight-elements array on the other side of the substrate has the same placement and separation between elements; thus, we excluded them for brevity. The mutual coupling of −22.8 dB was obtained between the closest antenna elements. The separation between the closest mm-wave elements was 2.5 mm, equivalent to a quarter wavelength at 28 GHz. Normally, the separation between antenna elements was half of the wavelength. Thus, placing the

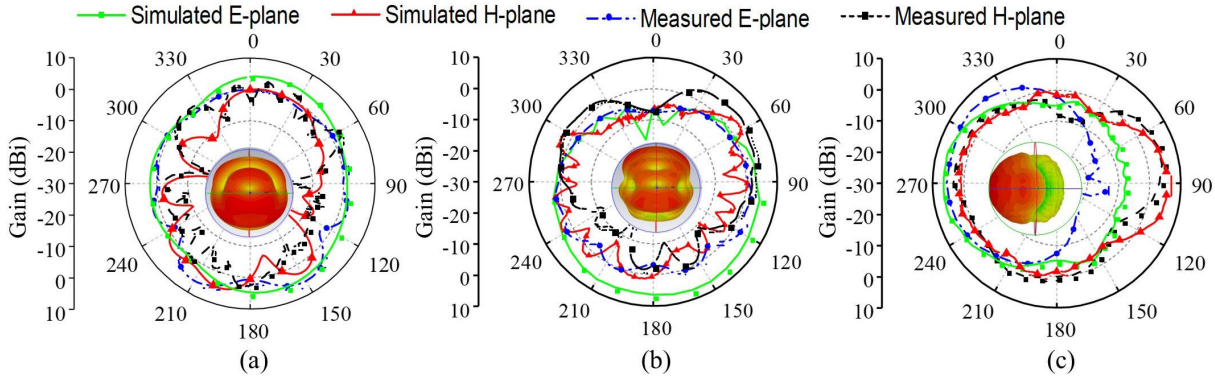

FIGURE 13. Comparison of simulated and measured polar radiation pattern with inset 3D patterns for (a) sub-6 GHz Ant-1 at 3.8 GHz, (b) sub-6 GHz Ant-1 at 5.4 GHz, and (c) antenna element-1 of mm-wave array-1 at 28 GHz..

TABLE 1. Gain and total efficiency of integrated antennas at different frequencies.

Frequency (GHz)	Antenna Elements	Gain (dBi)	Total efficiency(%)
3.8	Sub-6 GHz Ant-1	5.69	92.1
	Sub-6 GHz Ant-2	5.69	92.1
5.4	Sub-6 GHz Ant-1	5.05	78.39
	Sub-6 GHz Ant-2	5.05	78.36
28	Ant-1 of mm-wave array-1	6.24	95.1
	Ant- 2 of mm-wave array-1	6.12	94.8
	Ant-3 of mm-wave array-1	6.06	94.79
	Ant-4 of mm-wave array-1	6.06	94.76
	Ant-5 of mm-wave array-1	6.06	94.76
	Ant-6 of mm-wave array-1	6.06	94.76
	Ant-7 of mm-wave array-1	6.12	94.78
	Ant-8 of mm-wave array-1	6.24	95.29

elements very close, the proposed antenna can still provide adequate mutual coupling value at mm-wave frequencies. Similarly, the mutual coupling decreased drastically with other antenna elements i.e., becomes −43 and −45 dB as the separation increases. Furthermore, the parameters (specifically, $|S_{11}|$ and $|S_{21}|$ for brevity) of the mm-wave array were carefully measured with the fabricated prototypes shown in Fig. 6. The mm-wave antenna exhibited an impressive wide measured bandwidth of 1290 MHz, ranging from 27.38 to 28.67 GHz, with a notable $|S_{11}|$ depth of approximately -28 dB. The measured mutual coupling between the closest antenna elements (Ant-1 and Ant-2) was also recorded at -23.88 dB. Notably, measurements were performed on only a subset of elements because of the limited number of end-launch connectors and the similar behavior of antenna elements. Despite this constraint, the overall measured results exhibit a commendable alignment with the simulation results, affirming the accuracy and reliability of the proposed mm-wave array design.

In addition, the S-parameters of mm-wave antenna arrays near human body models, such as the head, chest, and hand, were also analyzed, as shown in Fig. 11. A slight shift in the resonance frequency at 28 GHz was observed when the

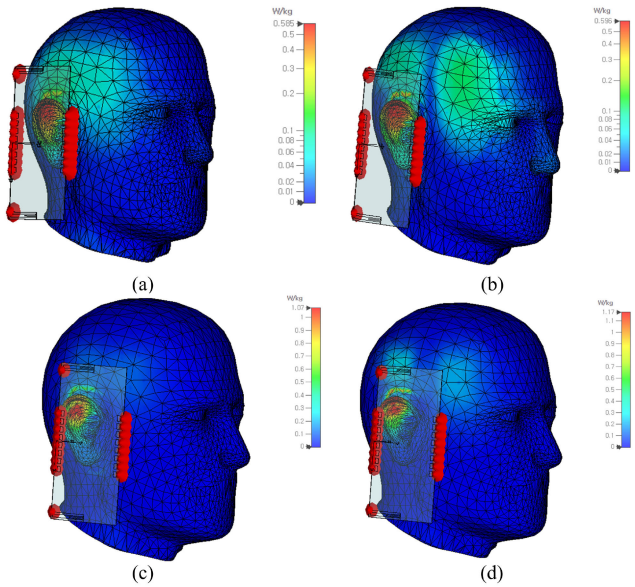

FIGURE 14. 1-g SAR distributions on human head model for (a) 3-cm distance at 3.8 GHz, (b) 3-cm distance at 5.4 GHz, (c) 1-cm distance at 3.8 GHz, and (d) 1-cm distance at 5.4 GHz.

antenna arrays were placed 1–3 cm away from the chest model with an $|S_{11}|$ depth of ~ -17 dB. Similarly, the head model inclusion near the antenna resulted in a small variation in the results due to high dielectric properties, while the $|S_{11}|$ depth was improved, which enhanced the bandwidth. Similarly, hand model inclusion provided adequate performance with an $|S_{11}|$ depth of ~ -26 dB. Moreover, the mutual coupling between the antenna elements in the array remained nearly the same as in free space, even after incorporating body models. However, a slight shift toward higher frequency was noted, but the proposed array exhibited an adequate −10 dB bandwidth of 1040 MHz (27.5–28.54 GHz), which can effectively cover the 28 GHz band.

D. FAR-FIELD RADIATION PERFORMANCE

The radiation performance of the proposed PIFA and mm-wave antennas was computed in the integrated form in

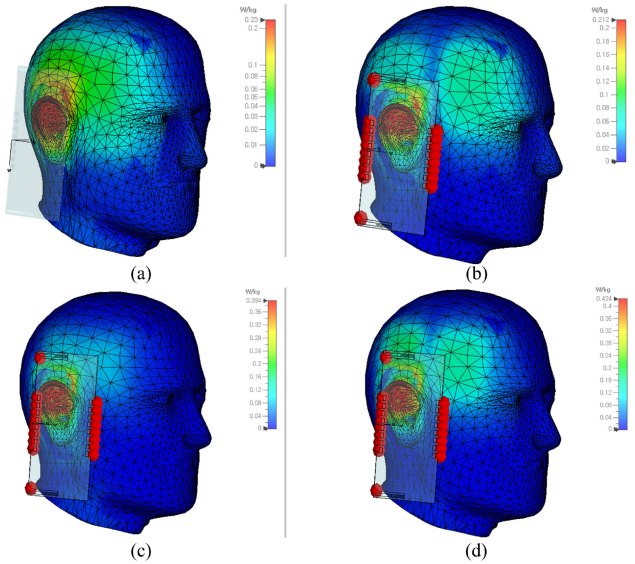

FIGURE 15. 10-g SAR distributions on human head model for (a) 3-cm distance at 3.8 GHz, (b) 3-cm distance at 5.4 GHz, (c) 1-cm distance at 3.8 GHz, and (d) 1-cm distance at 5.4 GHz.

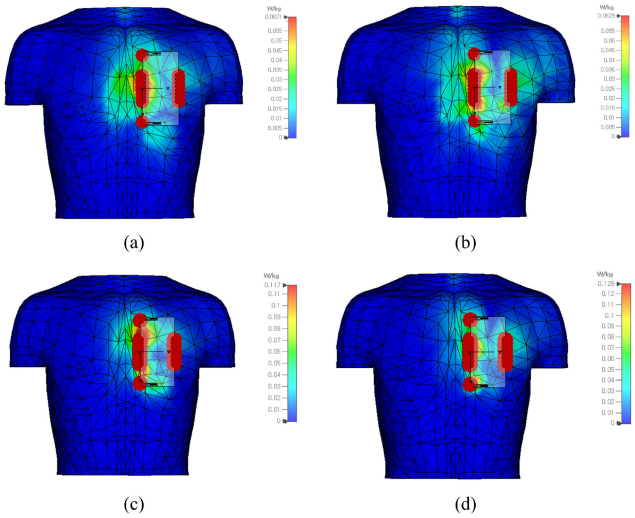

FIGURE 16. 1-g SAR distributions on human chest model positioned (a) 3-cm distance at 3.8 GHz, (b) 3-cm distance at 5.4 GHz, (c) 1-cm distance at 3.8 GHz, and (d) 1-cm distance at 5.4 GHz.

terms of efficiency, radiation pattern, and peak gain. The sub-6 GHz PIFA provides maximum efficiency of 92% and 78.4% in the sub-6 GHz 5G band and LTE band-46, respectively. The total efficiency of the mm-wave antenna arrays was in the range of 94.76%-95.3%. These efficiencies include losses such as mismatch, radiation, and mutual coupling. Table 1 enlisted the total efficiency and gain of each antenna element. Additionally, a comparative analysis of the total efficiency of the proposed antennas is illustrated in Fig. 12, which contains both measured and simulated data. Significantly, a high degree of agreement exists between the measured and simulated efficiencies at both the sub-6 GHz and mm-wave frequency bands, validating the accuracy and reliability of the presented results. Fig. 12 further compares the maximum simulated and measured gains across the frequency ranges in

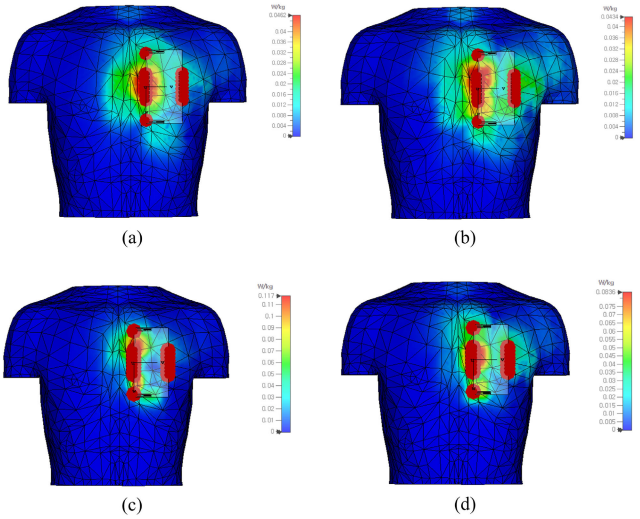

FIGURE 17. 10-g SAR distributions on human chest model positioned (a) 3-cm distance at 3.8 GHz, (b) 3-cm distance at 5.4 GHz, (c) 1-cm distance at 3.8 GHz, and (d) 1-cm distance at 5.4 GHz.

the sub-6 GHz and mm-wave frequencies. It is evident from Figs. 12(a) and 12(b) that the proposed antennas maintained adequate gain in both simulations and measurements within the bands of interest.

Figs. 13(a)–(c) portray the simulated and measured radiation patterns with inset 3D gain patterns of the proposed integrated sub-6 GHz and mm-wave antennas at 3.8, 5.4, and 28 GHz frequency bands, respectively. Owing to the symmetrical placement and equal separation of the antenna element, only the radiation patterns of the single element were measured and included here for brevity. However, the details of peak gain can be found in Table 1. The PIFA provides a peak simulated gain of 5.69 dBi at 3.8 GHz and 5.05 dBi at 5.4 GHz. However, the mm-wave single antenna element provides a 6.16 dBi peak gain with a directional radiation pattern at 28 GHz. The peak gains of all the mm-wave antenna array elements were in the range of 6.1–6.5 dBi.

E. SAFETY STUDY OF INTEGRATED SUB-6 GHZ AND MM-WAVE STRUCTURES

1) SPECIFIC ABSORPTION RATE

Owing to exposure to electromagnetic waves, smartphone antennas working near the human body are required to radiate within the safety limits. Because of ionization and temperature rise, the absorption of EM waves is harmful to the human body. Regarding EM exposure, international safety guidelines, such as IEEE and ICNRP, have been established. Based on these guidelines, the SAR restricts tissue heating due to the absorption of EM waves for frequencies less than 10 GHz. However, for the higher frequencies above 10 GHz, the regulations of PD near the body surface are imposed. The amount of power absorbed in the tissue can be denoted by Equation (1) [36].

$$\mathrm{SAR} = \frac{\sigma |E|^2}{2\rho} \tag{1}$$

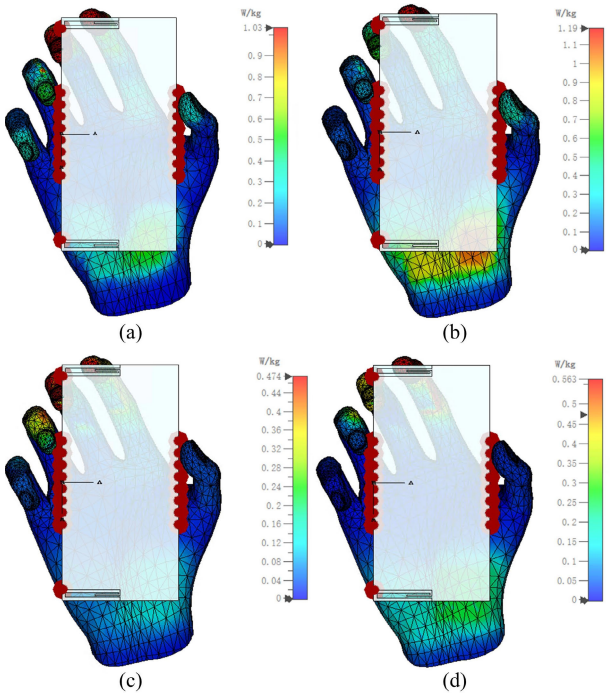

FIGURE 18. SAR analysis for the proposed integrated antennas in single-hand data mode: 1-g peak SAR distributions at (a) 3.8 GHz and (b) 5.4 GHz, and 10-g peak SAR distributions at (c) 3.8 GHz and (d) 5.4 GHz.

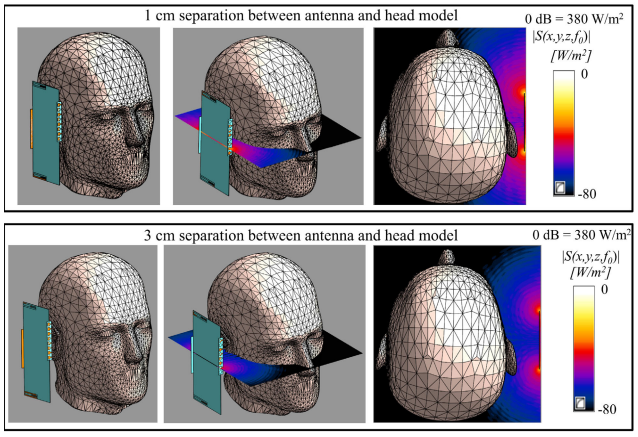

FIGURE 19. Simulation setups including PD distributions at 28 GHz; top row 1 cm and bottom 3 cm away from the head model in Sim4life software.

Here, the σ represents the conductivity of the tissue, and its unit is S/m, while the ρ denotes the density of the body tissues with a unit of kg/m^3, and the electric field strength was denoted by E (V/m). Thus, based on the IEEE and ICNRP, the SAR values should be kept under 1.6 or 2 W/kg for 1-g or 10-g of tissue, respectively [37]. The SAR of the proposed PIFA was simulated in CST microwave studio software in the head and torso model, and the antenna was kept 1 and 3 cm from the tissue. To analyze the safety of smartphone users during phone calls, it is advisable to evaluate safety with a human head model. This is particularly crucial as smartphones are close to the human head during such interactions. Furthermore, when

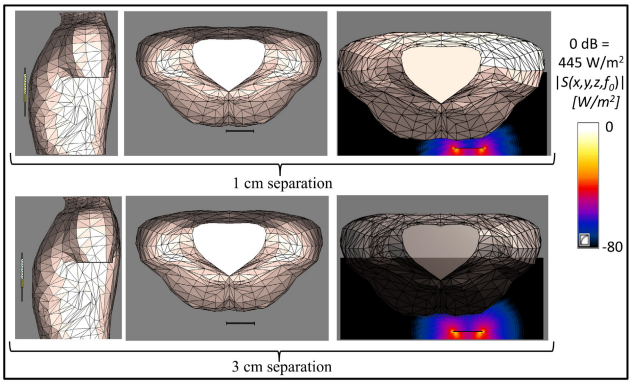

FIGURE 20. Simulation setups including PD distributions at 28 GHz; top row 1 cm and bottom 3 cm away from chest model in Sim4life software.

users place their smartphones in a chest pocket or utilize data services while lying down, the devices are close to the human chest. Consequently, we conducted SAR calculations in these specific scenarios. We have considered the input power of 24 dBm to the antenna during the simulation. The LTE usually utilizes 24 dBm of input power for safety evaluation; however, for 5G the input power regulations are not yet specified [38], [39]. Figs. 14(a)–(d) present the simulated 1-g SAR on the human head model for the PIFA. When the proposed antenna configuration was placed 3 cm from the head model, 1-g SAR values of 0.585 and 0.596 W/kg were observed at 3.8 and 5.4 GHz, respectively. Closer placement at 1 cm increased SAR to 1.07 and 1.17 W/kg at 3.8 and 5.4 GHz, respectively. However, in both scenarios, the 1-g SAR was much lower than the specified limits of IEEE. Figs. 15 (a)–(d) present the 10-g SAR for antenna-to-head model separations of 3 and 1 cm. At a 3-cm distance, the PIFA 10-g SARs were limited to 0.23 and 0.212 W/kg at 3.8 and 5.4 GHz, respectively. Furthermore, when the antennas were positioned 1 cm away from the human head for 10-g SAR evaluation, the values were 0.394 and 0.424 W/kg at 3.8 and 5.4 GHz, respectively. The proposed dual-band PIFA exhibited significantly low SAR values for both 3- and 1-cm distances.

Furthermore, we conducted SAR simulations for the chest utilizing identical configurations. Figs. 16(a)–(d) display the 1-g SAR values calculated at distances of 3 and 1 cm for the frequency bands of sub-6 GHz and LTE band-46. When the PIFA was positioned 3 cm from the torso model, the 1-g SAR values were 0.0621 and 0.0629 W/kg in the sub-6 GHz and LTE band-46, respectively. At a closer distance of 1 cm, the SAR values increased to 0.117 and 0.129 W/kg in the sub-6 GHz and LTE band-46, respectively. Fig. 17 portrays the 10-g SAR at 3.8 and 5.4 GHz frequency bands at 3 and 1 cm separations. The achieved 10-g SAR values at a 3 cm distance in the sub-6 GHz and LTE band-46 were 0.0462 and 0.0434 W/kg, respectively. Meanwhile, at 1 cm, the simulated SAR was 0.117 and 0.0836 W/kg for the sub-6 GHz and LTE band-46, respectively. The calculated SAR values for 1-g and 10-g limits were notably lower than those obtained with the head model. The net input power was consistently maintained

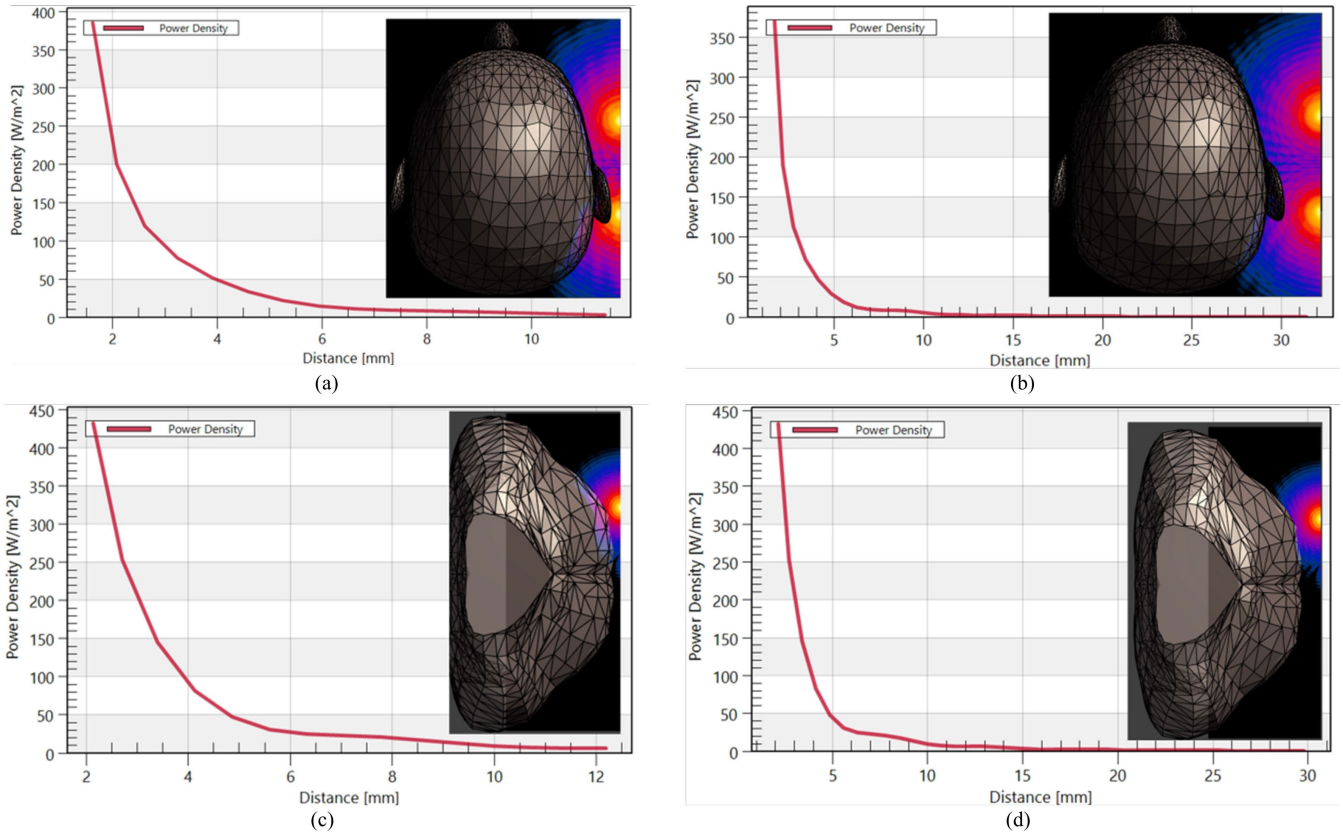

FIGURE 21. PD of proposed antenna array configurations at 28 GHz with (a) 1-cm separation from the head model, (b) 3-cm separation from the head model, (c) 1-cm separation from the torso model, and (d) 1-cm separation from the torso model.

TABLE 2. SAR analysis of integrated antenna for different sub-6 GHz frequencies, body models, and distances.

Frequency (GHz)	Body Model	Distance	1-g SAR	10-g SAR
3.8	Head	1 cm	1.07	0.394
		3 cm	0.585	0.23
	Chest	1 cm	0.117	0.117
		3 cm	0.0621	0.0462
5.4	Head	1 cm	1.17	0.424
		3 cm	0.596	0.212
	Chest	1 cm	0.129	0.0836
		3 cm	0.0629	0.0434

at 24 dBm throughout these simulations. Further details of the SAR calculations in all scenarios are provided in Table 2.

Additionally, we conducted a thorough SAR analysis for the single-hand data mode, as depicted in Fig. 18. In Figs. 18(a) and 18(b), 1-g peak SAR values of 1.03 and 1.19 W/kg were recorded at 3.8 and 5.4 GHz, respectively. However, for the 10-g SAR, the values reduced to 0.474 and 0.563 W/kg at 3.8 and 5.4 GHz in Figs. 18(c) and 18(d), respectively. The safety analysis across all scenarios with a net input power of 24 dBm confirms that the proposed integrated antennas are safe for use near human body tissues, and SAR is not a concern in this study. The achievement of consistently low SAR in all scenarios can be attributed to the utilization of a full system ground plane, effectively preventing back radiation toward the body.

2) POWER DENSITY

Another safety aspect is the PD, which is utilized to avoid heating the human body tissues at higher frequencies, particularly bands greater than 10 GHz. The main reason for calculating PD is the low penetration depth at higher frequencies; thus, the heating occurs only on the surface of the tissue [40]. We considered the head, hand, and torso models for talking and data modes by placing the integrated antenna at 1- and 3-cm distances. The numerical setup in Sim4life software and the PD distributions for the head model and chest model are shown in Figs. 19 and 20, respectively.

Figs. 21(a)-(d) illustrate the PDs of the proposed antenna array configurations at 28 GHz when placed at 3- and 1-cm distances to the head and torso model. Sim4life FDTD-based simulator is used to calculate the PD at a higher frequency, such as 28 GHz. For PD data extraction, 3- and 1-cm lines were drawn from the antenna elements to the surface of the body models. The same input power of 24 dBm was considered for PD evaluation. The proposed mm-wave antennas exhibited high PD (380 W/m^2 and 480 W/m^2 for head and torso, respectively) when they were close to the human models, and the PD level decreased by moving

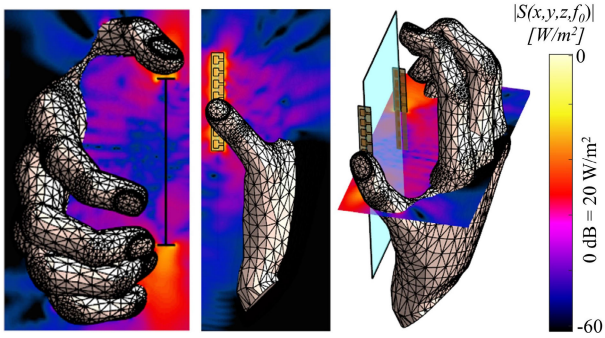

FIGURE 22. Analysis of the spatial PD distributions in data mode with hand model at 28 GHz.

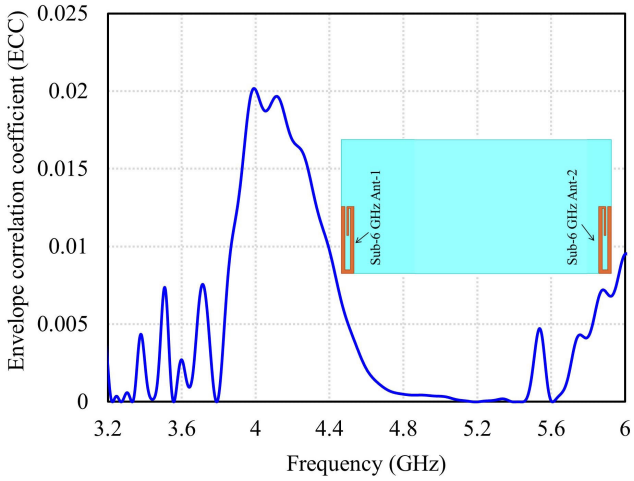

FIGURE 23. ECC between sub-6 GHz antennas i.e., Sub-6 GHz Ant-1 and Sub-6 GHz Ant-2.

antennas away from the models. Based on ICNIRP, FCC, and IEEE guidelines, the PD value on the surface of human body tissue should be less or equal to 10 W/m^2 [41]. As evident from Figs. 21(a)-(d), the proposed antenna elements provide minimal PD values on the surface of the head and torso models. Moreover, the PD for the data mode with a hand model was also analyzed at 28 GHz. The Sim4life software numerical setup including spatial PD distributions on the hand surface are depicted in Fig. 22. The highest PD values on the surfaces of the head, hand, and chest within all configurations adhered to the specified limit of 10 W/m^2 for an input power of 24 dBm. Based on the safety analysis, the integrated antenna system proposed in this paper ensures that SAR and PD values for the antenna system, deployed in various modes, remain within the standard range.

F. MIMO PARAMETERS AND BEAMFORIMING

Regardless of better isolation, low reflection, and enhanced radiation behavior, the main purpose of the MIMO formation is the diversity and multiplexing performance. Thus, investigating ECC and channel capacity is peculiarly important. The ECC value should be kept below 0.5 for enhanced MIMO performance with low coupling [18], [42]. We calculated the

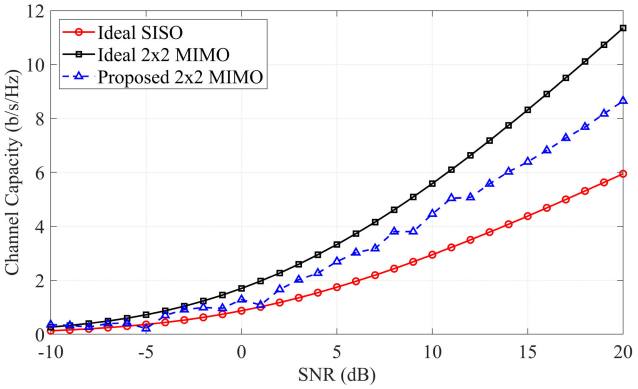

FIGURE 24. Channel capacities comparison - depicting the channel capacities under various SNRs for the proposed 2 × 2 MIMO antenna, in contrast to an ideal SISO configuration and an ideal 2 × 2 MIMO system.

ECC based on the radiation patterns of each antenna element utilizing Equation (2).

$$\rho_{ij} = \frac{|\int \int_0^{4\pi} [\vec{F}_i(\theta,\phi) \times \vec{F}_j(\theta,\phi) d\Omega]|^2}{\int \int_0^{4\pi} |\vec{F}_i(\theta,\phi)|^2 d\Omega \int \int_0^{4\pi} |\vec{F}_j(\theta,\phi)|^2 d\Omega}, \quad (2)$$

where the ECC is denoted by ρ_{ij}, while $\mathbf{F}_i(\theta,\phi)$ and $\mathbf{F}_j(\theta,\phi)$ denote the ith and jth antenna radiation patterns, respectively. $i, j = 1, 2, 3, \ldots, N$; N denotes the number of antenna elements in the MIMO configurations. Fig. 23 shows the calculated ECC between the sub-6 GHz elements (sub-6 GHz Ant-1 and sub-6 GHz Ant-2) of the 2 × 2 MIMO configuration. The ECC at 3.8 and 5.4 GHz was less than 0.01, which is much lower than the specified value of 0.5.

With the evolution of wireless communication, understanding and accurately describing channel resources through models has become crucial. MIMO systems, utilizing multiple antennas in both transmitter and receiver, enhance system performance and channel capacity compared to single input single output (SISO) systems [43]. Channel capacity is a key parameter in MIMO antenna systems, which is calculated based on the reported equations in [44]. Fig. 24 illustrates the calculated channel capacities at various signal-to-noise ratios (SNRs). The proposed antenna exhibits a notable enhancement in channel capacity compared to a SISO configuration; however, its capacity is slightly lower than the ideal 2 × 2 MIMO system.

In the rapidly evolving landscape of wireless communication technologies, 5G beam-steering is pivotal in advancing connectivity by enabling dynamic control of mm-wave beams. This crucial innovation enhances signal quality and coverage in mobile devices. To integrate the suggested antenna arrays into a 5G smartphone, dynamically adjusting the mm-wave beam over a broad scanning angle is essential [45]. In Fig. 25, the conceptual RF block diagram for beam steering is presented. It comprises essential components such as RF switches, power amplifiers (PA), low-noise amplifiers (LNA), power dividers/combiners, and phase shifters (PS). The beamforming attributes of the proposed antenna array are illustrated in Fig. 26. Beam-steering is

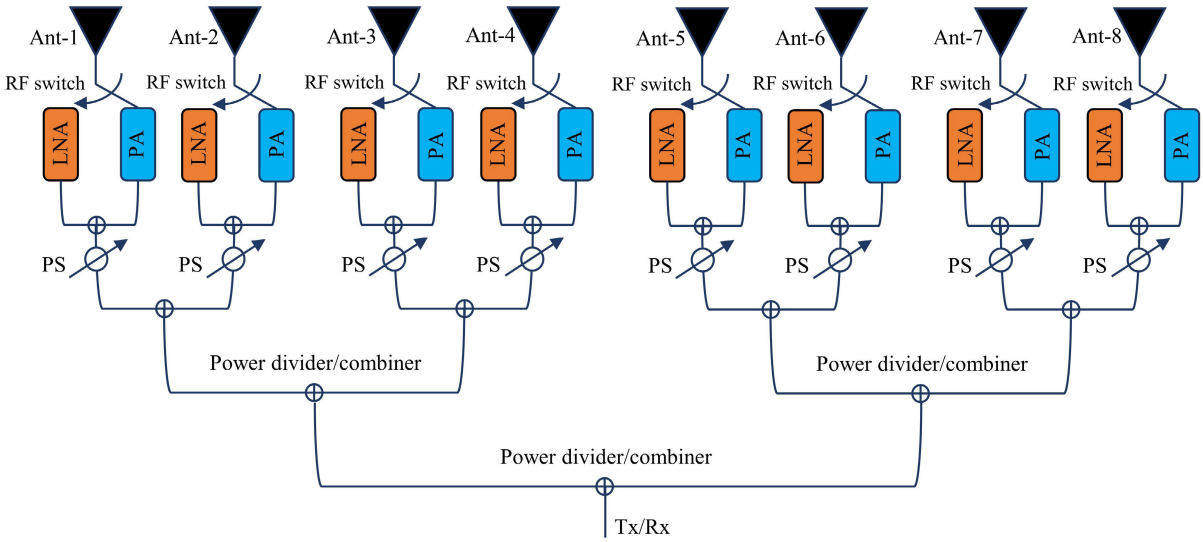

FIGURE 25. RF block diagram illustrating the beam steering process. Key components include RF switches, power amplifiers (PA), low-noise amplifiers (LNA), power dividers/combiners, and phase shifters (PS).

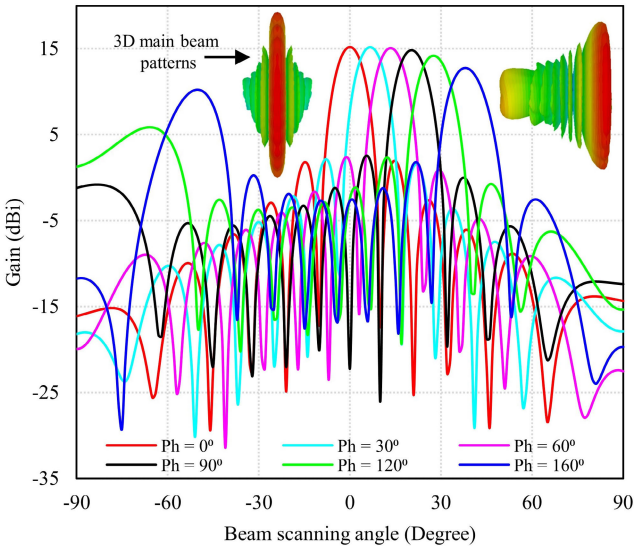

FIGURE 26. Illustration of 5G beamforming attributes in the proposed antenna array module. This figure shows dynamic beam-steering capabilities with controlled phase changes in antenna array elements, enabling scanning range from 0 to 160° with a gain of more than 10 dBi.

achieved via controlled changes in the phases of the antenna array elements feed. The presented array module exhibits an expansive scanning capability, covering a range of 0–160° degrees, while sustaining a consistently high gain exceeding 10 dBi. However, notably, achieving a wider beam scanning range comes at the expense of a gain reduction.

IV. CONCLUSION

This study introduces an integrated prototype meticulously designed to address the diverse frequency bands of sub-6 GHz (mid-band) and 5G mm-wave, specifically focusing on tailoring its capabilities for 4G LTE and 5G smartphone applications. The proposed design incorporates two distinctive configurations: a 2 × 2 MIMO arrangement for sub-6 GHz antennas on the short edges and two arrays of eight antenna elements on the long edges of the substrate for the mm-wave configuration. The design achieves optimal beamforming characteristics by strategically positioning these elements near a 2.5-mm separation, ensuring comprehensive coverage on both sides, mitigating interference with other applications, and achieving high gain and isolation. Utilizing a meandered patch structure and a truncated ground structure, the proposed dual-band PIFA attains a compact size of 37 mm × 7 mm × 0.508 mm, leveraging the Rogers RT/Duroid 5880 substrate. Operating effectively within the sub-6 GHz frequency bands, the design resonates at 3.8 GHz for 5G and 5.4 GHz for LTE band-46. Comprehensive safety analyses, including SAR assessment at sub-6 GHz bands and PD analysis at high-frequency bands, demonstrate adherence to safety restrictions set by the IEEE and the ICNIRP, with consistently lower PDs and SARs.

Furthermore, the design demonstrates efficient operation in the challenging 5G mm-wave band at 28 GHz. Beyond its extensive bandwidth coverage, the proposed architecture underwent thorough scrutiny to assess single and MIMO antenna performance. The antenna's high-performance parameters, combined with its adept MIMO characteristics, position the proposed design as a promising solution for contemporary smartphone applications. it adeptly meets the intricate requirements of both sub-6 GHz and 5G mm-wave frequencies. The successful realization of these objectives underscores the potential of the proposed prototype to contribute significantly to the advancement of wireless communication technologies for next-generation mobile devices.

ACKNOWLEDGMENT

(Ayesha Kazmi, Muhammad Zada, and Saiful Islam are co-first authors.)

REFERENCES

[1] M. Zada, I. A. Shah, and H. Yoo, "Integration of sub-6-GHz and mm-wave bands with a large frequency ratio for future 5G MIMO applications," *IEEE Access*, vol. 9, pp. 11241–11251, 2021.

[2] M. Abdullah, S. H. Kiani, and A. Iqbal, "Eight element multiple-input multiple-output (MIMO) antenna for 5G mobile applications," *IEEE Access*, vol. 7, pp. 134488–134495, 2019.

[3] G. Naik, J.-M. Park, J. Ashdown, and W. Lehr, "Next generation Wi-Fi and 5G NR-U in the 6 GHz bands: Opportunities and challenges," *IEEE Access*, vol. 8, pp. 153027–153056, 2020.

[4] J. G. Andrews, S. Buzzi, W. Choi, S. V. Hanly, A. Lozano, A. C. K. Soong, and J. C. Zhang, "What will 5G be?" *IEEE J. Sel. Areas Commun.*, vol. 32, no. 6, pp. 1065–1082, Jun. 2014.

[5] Federal Communications Commission. *America's 5G Future*. Accessed: Nov. 5, 2023. [Online]. Available: https://www.fcc.gov/5G

[6] A. Ghaffar, X. J. Li, W. A. Awan, S. Iffat Naqvi, N. Hussain, B.-C. Seet, M. Alibakhshikenari, F. Falcone, and E. Limiti, "Design and realization of a frequency reconfigurable multimode antenna for ISM, 5G-sub-6-GHz, and S-band applications," *Appl. Sci.*, vol. 11, no. 4, p. 1635, Feb. 2021.

[7] N. Jaglan, S. D. Gupta, B. K. Kanaujia, and M. S. Sharawi, "10 element sub-6-GHz multi-band double-T based MIMO antenna system for 5G smartphones," *IEEE Access*, vol. 9, pp. 118662–118672, 2021.

[8] M. A. Salamin, N. Hussain, and T. T. Le, "A 2 × 1 array-based wideband mm-wave antenna integrated with a 2-element multiple-input-multiple-output antenna for 5G mobile terminals," *Int. J. RF Microw. Comput.-Aided Eng.*, vol. 31, no. 8, Aug. 2021, Art. no. e22709.

[9] S. F. Jilani and A. Alomainy, "Millimetre-wave T-shaped MIMO antenna with defected ground structures for 5G cellular networks," *IET Microw., Antennas Propag.*, vol. 12, no. 5, pp. 672–677, Apr. 2018.

[10] W. A. Awan, Halima, A. Zaidi, N. Hussain, S. Khalid, and A. Baghdad, "Characterization of dual band MIMO antenna for 25 GHz and 50 GHz applications," in *Proc. Int. Conf. Comput., Electron. Electr. Eng. (ICE Cube)*, Nov. 2018, pp. 1–4.

[11] J.-F. Li, D.-L. Wu, B. Huang, and Y.-J. Wu, "A LTE smartphone antenna with an internal matching circuit to cover 698–2710 MHz," *Microw. Opt. Technol. Lett.*, vol. 59, no. 9, pp. 2405–2411, Sep. 2017.

[12] S. Islam, M. Zada, and H. Yoo, "Low-pass filter based integrated 5G smartphone antenna for sub-6-GHz and mm-wave bands," *IEEE Trans. Antennas Propag.*, vol. 69, no. 9, pp. 5424–5436, Sep. 2021.

[13] C. Dehos, J. L. González, A. De Domenico, D. Kténas, and L. Dussopt, "Millimeter-wave access and backhauling: The solution to the exponential data traffic increase in 5G mobile communications systems?" *IEEE Commun. Mag.*, vol. 52, no. 9, pp. 88–95, Sep. 2014.

[14] Y.-L. Ban, C. Li, C.-Y.-D. Sim, G. Wu, and K.-L. Wong, "4G/5G multiple antennas for future multi-mode smartphone applications," *IEEE Access*, vol. 4, pp. 2981–2988, 2016.

[15] Y. Li, C.-Y.-D. Sim, Y. Luo, and G. Yang, "12-port 5G massive MIMO antenna array in sub-6GHz mobile handset for LTE bands 42/43/46 applications," *IEEE Access*, vol. 6, pp. 344–354, 2018.

[16] S. I. Naqvi, A. H. Naqvi, F. Arshad, M. A. Riaz, M. A. Azam, M. S. Khan, Y. Amin, J. Loo, and H. Tenhunen, "An integrated antenna system for 4G and millimeter-wave 5G future handheld devices," *IEEE Access*, vol. 7, pp. 116555–116566, 2019.

[17] J. Kurvinen, H. Kähkönen, A. Lehtovuori, J. Ala-Laurinaho, and V. Viikari, "Co-designed mm-wave and LTE handset antennas," *IEEE Trans. Antennas Propag.*, vol. 67, no. 3, pp. 1545–1553, Mar. 2019.

[18] W. C. Mok, S. H. Wong, K. M. Luk, and K. F. Lee, "Single-layer single-patch dual-band and triple-band patch antennas," *IEEE Trans. Antennas Propag.*, vol. 61, no. 8, pp. 4341–4344, Aug. 2013.

[19] J. Zhu, M. A. Antoniades, and G. V. Eleftheriades, "A compact tri-band monopole antenna with single-cell metamaterial loading," *IEEE Trans. Antennas Propag.*, vol. 58, no. 4, pp. 1031–1038, Apr. 2010.

[20] X. L. Sun, S. W. Cheung, and T. I. Yuk, "Dual-band monopole antenna with frequency-tunable feature for Wimax applications," *IEEE Antennas Wireless Propag. Lett.*, vol. 12, pp. 100–103, 2013.

[21] U. Deepak, T. K. Roshna, C. M. Nijas, K. Vasudevan, and P. Mohanan, "A dual band SIR coupled dipole antenna for 2.4/5.2/5.8 GHz applications," *IEEE Trans. Antennas Propag.*, vol. 63, no. 4, pp. 1514–1520, Apr. 2015.

[22] V.-A. Nguyen, B.-Y. Park, S.-O. Park, and G. Yoon, "A planar dipole for multiband antenna systems with self-balanced impedance," *IEEE Antennas Wireless Propag. Lett.*, vol. 13, pp. 1632–1635, 2014.

[23] M. A. Antoniades and G. V. Eleftheriades, "Multiband compact printed dipole antennas using NRI-TL metamaterial loading," *IEEE Trans. Antennas Propag.*, vol. 60, no. 12, pp. 5613–5626, Dec. 2012.

[24] M. Ikram, E. A. Abbas, N. Nguyen-Trong, K. H. Sayidmarie, and A. Abbosh, "Integrated frequency-reconfigurable slot antenna and connected slot antenna array for 4G and 5G mobile handsets," *IEEE Trans. Antennas Propag.*, vol. 67, no. 12, pp. 7225–7233, Dec. 2019.

[25] Y. F. Cao, S. W. Cheung, and T. I. Yuk, "A multiband slot antenna for GPS/WiMAX/WLAN systems," *IEEE Trans. Antennas Propag.*, vol. 63, no. 3, pp. 952–958, Mar. 2015.

[26] C.-K. Hsu and S.-J. Chung, "Compact antenna with U-shaped open-end slot structure for multi-band handset applications," *IEEE Trans. Antennas Propag.*, vol. 62, no. 2, pp. 929–932, Feb. 2014.

[27] C.-H. Chang and K.-L. Wong, "Printed λ/8-PIFA for penta-band WWAN operation in the mobile phone," *IEEE Trans. Antennas Propag.*, vol. 57, no. 5, pp. 1373–1381, May 2009.

[28] Y. Liu, Y. Li, L. Ge, J. Wang, and B. Ai, "A compact hepta-band mode-composite antenna for sub (6, 28, and 38) GHz applications," *IEEE Trans. Antennas Propag.*, vol. 68, no. 4, pp. 2593–2602, Apr. 2020.

[29] M. Ikram, N. Nguyen-Trong, and A. Abbosh, "Multiband MIMO microwave and millimeter antenna system employing dual-function tapered slot structure," *IEEE Trans. Antennas Propag.*, vol. 67, no. 8, pp. 5705–5710, Aug. 2019.

[30] M. Zada and H. Yoo, "A miniaturized triple-band implantable antenna system for bio-telemetry applications," *IEEE Trans. Antennas Propag.*, vol. 66, no. 12, pp. 7378–7382, Dec. 2018.

[31] S. Shamoon, W. Y. Zhou, F. Shahzad, W. Ali, and H. Subbyal, "Integrated sub-6 GHz and millimeter wave band antenna array modules for 5G smartphone applications," *AEU Int. J. Electron. Commun.*, vol. 161, Mar. 2023, Art. no. 154542.

[32] Y. Li, C.-Y.-D. Sim, Y. Luo, and G. Yang, "High-isolation 3.5 GHz eight-antenna MIMO array using balanced open-slot antenna element for 5G smartphones," *IEEE Trans. Antennas Propag.*, vol. 67, no. 6, pp. 3820–3830, Jun. 2019.

[33] M. E. Yassin, H. A. Mohamed, E. A. F. Abdallah, and H. S. El-Hennawy, "Single-fed 4G/5G multiband 2.4/5.5/28 GHz antenna," *IET Microw., Antennas Propag.*, vol. 13, no. 3, pp. 286–290, Feb. 2019.

[34] A. Basir, S. Ullah, M. Zada, and S. Faisal, "Design of efficient and flexible patch antenna using an electromagnetic band gap (EBG) ground plane," in *Proc. Int. Conf. Open Source Syst. Technol.*, Dec. 2014, pp. 1–5.

[35] Y. Sagae, S. Sawamukai, Y. Ohwatari, K. Kiyoshima, K. Kanbara, and J. Takahashi, "5G network," *NTT DOCOMO Tech. J.*, vol. 22, no. 2, pp. 23–39, 2020.

[36] M. El Halaoui, A. Kaabal, H. Asselman, S. Ahyoud, and A. Asselman, "Multiband planar inverted-F antenna with independent operating bands control for mobile handset applications," *Int. J. Antennas Propag.*, vol. 2017, pp. 1–13, Mar. 2017.

[37] M. Yousaf, I. B. Mabrouk, M. Zada, A. Akram, Y. Amin, M. Nedil, and H. Yoo, "An ultra-miniaturized antenna with ultra-wide bandwidth characteristics for medical implant systems," *IEEE Access*, vol. 9, pp. 40086–40097, 2021.

[38] J. Bang and J. Choi, "A SAR reduced mm-wave beam-steerable array antenna with dual-mode operation for fully metal-covered 5G cellular handsets," *IEEE Antennas Wireless Propag. Lett.*, vol. 17, pp. 1118–1122, 2018.

[39] S. Islam, M. Zada, and H. Yoo, "Highly compact integrated sub-6 GHz and millimeter-wave band antenna array for 5G smartphone communications," *IEEE Trans. Antennas Propag.*, vol. 70, no. 12, pp. 11629–11638, Dec. 2022.

[40] T. Wu, T. S. Rappaport, and C. M. Collins, "Safe for generations to come: Considerations of safety for millimeter waves in wireless communications," *IEEE Microw. Mag.*, vol. 16, no. 2, pp. 65–84, Mar. 2015.

[41] S. I. Naqvi, N. Hussain, A. Iqbal, M. Rahman, M. Forsat, S. S. Mirjavadi, and Y. Amin, "Integrated LTE and millimeter-wave 5G MIMO antenna system for 4G/5G wireless terminals," *Sensors*, vol. 20, no. 14, p. 3926, Jul. 2020.

[42] A. Iqbal, A. Basir, A. Smida, N. K. Mallat, I. Elfergani, J. Rodriguez, and S. Kim, "Electromagnetic bandgap backed millimeter-wave MIMO antenna for wearable applications," *IEEE Access*, vol. 7, pp. 111135–111144, 2019.

[43] W. Jiang, Y. Cui, B. Liu, W. Hu, and Y. Xi, "A dual-band MIMO antenna with enhanced isolation for 5G smartphone applications," *IEEE Access*, vol. 7, pp. 112554–112563, 2019.
[44] S. M. A. Shah, M. Zada, J. Nasir, O. Owais, A. Iqbal, and H. Yoo, "Miniaturized four-port MIMO implantable antenna for high-data-rate wireless-capsule-endoscopy applications," *IEEE Trans. Antennas Propag.*, vol. 71, no. 4, pp. 3123–3133, Apr. 2023.
[45] S. Islam, M. Zada, and H. Yoo, "Low-profile PIN-diode-controlled bezel fit radiation-pattern reconfigurable antenna arrays for 5G smartphones," *IEEE Trans. Antennas Propag.*, vol. 71, no. 8, pp. 6470–6480, Nov. 2023.

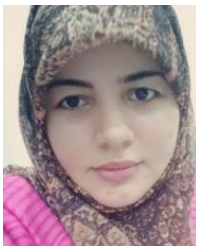

AYESHA KAZMI received the B.S. degree in electrical (telecommunication) engineering from COMSATS University Islamabad, Pakistan, in 2016, and the M.S. degree in electrical engineering (communication) from the CECOS University of IT and Emerging Sciences, Pakistan, in 2022. She joined the Department of Electrical Engineering, CECOS University of IT and Emerging Sciences, in 2016. Her current research interests include wearable sensors and antennas, millimeter wave antennas, MIMO antennas, and other RF front-end components.

MUHAMMAD ZADA (Member, IEEE) received the B.Sc. degree in telecommunication engineering from the University of Engineering and Technology, Peshawar, Pakistan, in 2015, and the integrated M.S./Ph.D. degree in electronic engineering from Hanyang University, Seoul, South Korea, in 2023.

From March 2023 to September 2023, he was a Postdoctoral Researcher with Hanyang University. Since September 2023, he has been a Postdoctoral Fellow with Shenzhen University, Shenzhen, China, where he continues to conduct research in the field of electronic and biomedical engineering. He has published over 30 papers in high-quality journals and conference proceedings. His current research interests include implantable antennas and devices, intra-oral tongue drive systems, wireless power transfer, energy harvesting, smart-textile, millimeter-wave antennas, MIMO antennas, frequency and pattern reconfigurable antennas, wearable sensors and antennas, microwave breast cancer detection, metamaterials, and electromagnetic bandgap structures.

Dr. Zada received the Best Student Paper Competition 2018 Award from Korean Institute of Electromagnetic Engineering and Science (KIEES). During the Ph.D. studies at Hanyang University, he was honored with the Best Ph.D. Thesis Award. He is currently serving as a Reviewer for several IEEE TRANSACTIONS, *International Journal of RF and Microwave Computer-Aided Engineering* (RFCAD), and Elsevier journals.

SAIFUL ISLAM (Graduate Student Member, IEEE) was born in Dhaka, Bangladesh, in 1996. He received the B.Sc. degree in electrical and electronic engineering from Daffodil International University, in 2018. He is currently pursuing the combined M.S. and Ph.D. degree in electronic engineering with Hanyang University, Seoul, South Korea.

His research interests include 5G communications, RF energy harvesting, microwave circuits, implantable antennas and systems, wearable electronics, the finite element method (FEM) for electromagnetics, multi-input–multi-output (MIMO) communication, reconfigurable antennas, microwave imaging, wireless charging of biomedical implants, magnetic resonance imaging (MRI), and RF coils.

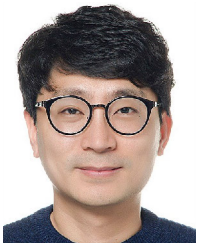

HYOUNGSUK YOO (Senior Member, IEEE) received the B.Sc. degree in electrical engineering from Kyungpook National University, Daegu, South Korea, in 2003, and the M.Sc. and Ph.D. degrees in electrical engineering from the University of Minnesota, Minneapolis, MN, USA, in 2006 and 2009, respectively.

In 2009, he joined the Center for Magnetic Resonance Research, University of Minnesota, as a Postdoctoral Associate. In 2010, he joined Cardiac Rhythm Disease Management, Medtronic, MN, USA, as a Senior EM/MRI Scientist. From 2011 to 2018, he was an Associate Professor with the Department of Biomedical Engineering, School of Electrical Engineering, University of Ulsan, Ulsan, South Korea. Since 2018, he has been a Full Professor with the Department of Biomedical Engineering and the Department of Electronic Engineering, Hanyang University, Seoul, South Korea. He has been the CEO of E2MR, Seoul, a startup company, since 2017. His current research interests include electromagnetic theory, numerical methods in electromagnetics, metamaterials, antennas, implantable devices, and magnetic resonance imaging in high-magnetic field systems.

Dr. Yoo was awarded the Third Prize for the Best Student Paper at the 2010 IEEE Microwave Theory and Techniques Society International Microwave Symposium.